thermo

MDPI

Article

Modeling Magnetic Hyperthermia of ZnO:Fe_3O_4:Chitosan Nanocomposites in Perfused Tumor Tissue

Ioan Albert Tudor [1,*], Liviu Badea [1,*], Miruna Adriana Iota [1], Marian Nicolae Costea [1,2], Ana Maria Mocioiu [1] and Adrian Mihail Motoc [1]

[1] National Research and Development Institute of Non-Ferrous and Rare Metals, 178-184 Biruintei Blvd, 077145 Pantelimon, Romania; iota.miruna@imnr.ro (M.A.I.); mcostea@imnr.ro (M.N.C.); ammocioiu@imnr.ro (A.M.M.); amotoc@imnr.ro (A.M.M.)

[2] Faculty of Materials Science and Engineering, National University of Science and Technology POLITEHNICA Bucharest, 060042 Bucharest, Romania

* Correspondence: atudor@imnr.ro (I.A.T.); lbadea@imnr.ro (L.B.)

Abstract

Magnetic hyperthermia models often use arbitrarily chosen or post hoc adjusted inputs, which obscures what determines tumor heating and thermal dose. In the present MATLAB model, every input is traced to a published measurement and the heat source is computed, not prescribed. A temperature-dependent two-level model of the non-linear Stoner–Wohlfarth hysteresis of immobilized magnetite cores is coupled to the Pennes bioheat equation and to the CEM43 thermal dose, for spheres with the volumes of pediatric CNS neuroblastoma (FOXR2-activated) under the glioblastoma clinical protocol. Monte Carlo and Sobol analyses over literature bounds identify the controlling inputs. At the clinical dose, the ZnO:Fe_3O_4:chitosan mass ratio does not affect the heat source, because only the magnetic phase generates heat. Linear response theory overestimates the loss by 63% at the Atkinson–Brezovich (AB) field. A median of 43 °C in a 115 mL tumor requires about 4.9 kA m^{-1}, whereas the center of a 10.5 mL lesion stays below 43 °C at the AB field. The reported range of the Néel attempt time can reduce the loss of monodisperse cores a hundredfold, whereas the reported size spread triples it; over these bounds, the median temperature at the AB field spans 37–59 °C (5th–95th percentiles).

Keywords: magnetic hyperthermia; dynamic hysteresis; Pennes bioheat equation; CEM43 thermal dose; uncertainty quantification; ZnO–Fe_3O_4/chitosan nanocomposite

Academic Editors: Jian Liu and Yiheng Tong

Received: 30 September 2026
Revised: 23 October 2026
Accepted: 27 October 2026
Published: 3 November 2026

Copyright: © 2026 by the authors. Licensee MDPI, Basel, Switzerland. This article is an open access article distributed under the terms and conditions of the Creative Commons Attribution (CC BY) license.

1. Introduction

Magnetic hyperthermia has been applied to patients with recurrent glioblastoma through intratumoral delivery of an aminosilane-coated iron oxide fluid followed by exposure to a 100 kHz field [1]. Measured temperatures varied widely, with a median intratumoral peak of 51.2 °C [1], and recent reviews highlight particle distribution, thermometry, and treatment planning as major challenges for clinical translation [2–4]. In pediatric oncology, hyperthermia holds promise as a radiosensitizer that could reduce radiation doses to the immature brain, and patient-specific applicators are designed with bioheat-transfer models [5]. Magnetite dispersed in chitosan-based hydrogels is being developed for magnetic hyperthermia [6]; and ZnO nanoparticles interfere with zinc

metabolism in SH-SY5Y neuroblastoma cells [7], a subclone of a cell line derived from a bone-marrow metastasis of peripheral neuroblastoma [8]. Model simulations typically adopt parameters from independent reports or fit them until a desired outcome is achieved; physical effects are then difficult to distinguish from arbitrary input choices. An easily overlooked constraint is that, at clinically administered iron doses, heat is generated by the magnetic phase alone; nonmagnetic constituents contribute only indirectly, through their thermal properties. Moreover, ZnO dissolution is solubility-limited: in cell-culture medium at 37 °C, the oxide dissolves completely only up to about 5.5 μg mL^{-1}, which is consistent with the formation of zinc carbonate [9]. Magnetic losses are commonly estimated using the classical Rosensweig formulation, derived from linear response theory (LRT), which requires the Zeeman energy to remain small compared with the thermal energy [10,11]. Hysteretic models based on the Stoner–Wohlfarth energy landscape or on thermally activated switching do not require this condition, and kinetic Monte Carlo simulations show that LRT fails at medically relevant amplitudes and particle sizes [11–14]. Cores of about 15 nm are therefore expected to leave the LRT regime at clinical amplitudes. Furthermore, the Néel anisotropy barrier should be evaluated in the absence of dipolar contributions, a condition that can be approached by extrapolating AC susceptibility measurements to infinite interparticle separation [15]. Magnetic losses depend on the environment and on temperature: they decrease when the particles are immobilized or internalized by cells [16,17] and change during heating itself [18]. On the heat-transfer side, the Pennes equation [19] and solutions for spherical heat sources [20] show that perfusion and geometry set the local temperature profile. Thermal dose is usually expressed as cumulative equivalent minutes at 43 °C (CEM43), but a model linking magnetic heat losses to a predicted CEM43 profile has, to our knowledge, not been reported for composite materials. Coupled magnetic–bioheat models exist [21,22], but they usually take the heat source from LRT or from a fitted specific absorption rate (SAR) and do not trace each input to a measurement. The present framework differs from these models in three respects. (i) The heat source is computed, not prescribed: the non-linear two-level dynamic hysteresis of immobilized magnetite cores yields an SAR that depends on the local temperature and is coupled to the Pennes equation, so the validity limit of LRT at clinical amplitudes follows from the model. (ii) The composite is split into the magnetic phase, which generates heat, and the other constituents, which act only through heat transport; at a fixed clinical iron dose, this separates the effect of composition from that of perfusion and allows compositions to be screened numerically before synthesis. (iii) All physical inputs are taken from published experimental studies, and the computation stops if an input is missing or differs from a fixed reference database; the temperature field is converted into CEM43 coverage, and a literature-bounded Monte Carlo and Sobol analysis identifies which measurable quantities, such as the Néel attempt time, control these predictions. The individual components are established; the contribution lies in coupling them in one chain whose inputs can be audited. The framework is applied to a sphere with the volumes reported for CNS neuroblastoma, FOXR2-activated (CNS NB-FOXR2), a pediatric intracranial tumor that was supratentorial and infiltrated the white matter in all 25 cases of a multi-institutional cohort [23]. As no individual study fully defines the magnetic, thermal, and clinical behavior of ZnO:Fe_3O_4:chitosan composites, the input parameters form a composite case study, in which the intracranial geometry comes from CNS NB-FOXR2 and the in vitro benchmarks from SH-SY5Y cells. We use the framework to explore how the composition affects heating at clinically applied iron doses, which amplitude is required to reach therapeutic temperatures and thermal-dose coverage, and which literature-derived parameters control the predictions.

https://doi.org/10.3390/thermo6040082

2. Results

2.1. Literature-Derived Model Inputs

The inputs (Table 1) fall into three groups. The magnetic group determines the heat source. It comprises iron oxide cores with a diameter of 15.3 nm and an effective anisotropy determined in the absence of dipolar interactions [15], the saturation magnetization and density of magnetite [10,24], and the Néel attempt time, the prefactor of the relaxation time. The attempt time has not been measured for cores of this size; its upper literature value is used in the base case and its lower value in the sensitivity analysis [25]. The clinical group fixes the dose and the field. The iron concentration of the injected fluid, the fluid volume per unit tumor volume, the frequency, the amplitude range and the heating time were adopted from a clinical glioblastoma study with aminosilane-coated magnetic nanoparticles [1]; the first two set the magnetite concentration in the tumor (Section 4.1). The thermal group determines how the deposited heat is removed. Volumes of 115 and 10.5 mL correspond to the mean and the second-smallest values among 25 CNS NB-FOXR2 tumors [23]. The thermal conductivity is 89% of that of water at 37 °C [26], the ratio measured for neuroblastoma cells [27]. The other tissue properties, which have not been measured for neuroblastoma, and those of the white-matter host were taken from a pediatric medulloblastoma treatment-planning study [5]. Perfusion and conductivity together set the perfusion length, which decides whether a lesion is perfusion- or conduction-limited (Section 2.3). The relative cerebral blood flow measured in a single CNS NB-FOXR2 patient [28], converted with the density and specific heat of blood [29], gives a perfusion coefficient close to the adopted value; this comparison serves only as a consistency check. The exposure criteria of Atkinson–Brezovich and Hergt–Dutz [30–32] bound the product $H_0 f$; they were established for the trunk and proposed for smaller body regions, respectively, and serve as reference exposure levels rather than safety guarantees. The applicator range extends above the first but stays below the second; at 100 kHz, the first corresponds to H_{AB} = 4.85 kA m^{-1}.

Table 1. Essential model parameters. Values in parentheses are the alternative literature values used in the sensitivity analysis.

Symbol	Meaning	Value	Unit	Source/Reference
D	Magnetic core diameter	15.3	nm	[15]
K_{eff}	Effective uniaxial anisotropy, corrected for dipolar interactions (AC field 1 Oe; 10 Oe in parentheses)	11.7 (11.9)	kJ m^{-3}	[15]
M_s	Saturation magnetization of magnetite	446	kA m^{-1}	[10,24]
ρ_{Fe3O4}	Density of magnetite	5180	kg m^{-3}	[10,24]
τ_0	Néel attempt time (upper literature bound; lower bound in parentheses)	10^{-9} (10^{-11})	s	[25]
SAR$_{fl}$	Reported SAR of the fluid characterized with the clinical applicator (about 21 mT, 100 kHz	35	W g^{-1} Fe	[33], as given in [34]
f	Frequency	100	kHz	[1]
H_0	Amplitude range of the applicator in the clinical study	2–15	kA m^{-1}	[1]
$H_0 f$	Atkinson–Brezovich (AB) and Hergt–Dutz (HD) exposure criteria	4.85×10^8 (AB); 5×10^9 (HD)	A m^{-1} s^{-1}	[30–32]
$c_{Fe,fl}$; d	Iron concentration of the clinical fluid; median fluid dose	112; 0.28	kg m^{-3}; mL cm^{-3}	[1]
$V_{inj,max}$	Largest fluid volume injected in the clinical protocol (dosing check)	11.6	mL	[1]

C_{Fe3O4}	Tumor-average Fe_3O_4 concentration (derived)	43.3	kg m^{-3}	Methods
t_{on}	Heating time	60	min	[1]
V (R_t)	Volume of CNS NB-FOXR2 (equivalent-sphere radius)	115 (30.2); 10.5 (13.6)	mL (mm)	[23]
ρ, c_p, k, ωC_b	Tumor density, specific heat, thermal conductivity, perfusion coefficient	1056; 3700; 0.56; 22 545	kg m^{-3}; J kg^{-1} K^{-1}; W m^{-1} K^{-1}; W m^{-3} K^{-1}	ρ, c_p, ωC_b: [5]; k: [26,27]
k_w	Thermal conductivity of water at 37 °C (reference for k)	0.6252	W m^{-1} K^{-1}	[26]
k/k_w	Conductivity ratio of neuroblastoma tumor cells to water (measured at 25, 37 and 44 °C); k = 0.89 × 0.6252	0.89	–	[27]
r_{CBF}	Relative cerebral blood flow in one CNS NB-FOXR2 patient (perfusion consistency check, not an input)	34.143	mL (100 g)$^{-1}$ min^{-1}	[28]
ρ_b; c_b	Blood density; specific heat (convert rCBF to $\omega C_b \approx 22.8$ kW m^{-3} K^{-1})	1050; 3617	kg m^{-3}; J kg^{-1} K^{-1}	[29]
ρ, c_p, k, ωC_b	White-matter host, same quantities	1038; 3600; 0.50; 15 925	as above	[5]
T_a	Arterial and baseline temperature	37	°C	[21]
R	CEM43 base for $T \geq 43$ °C; $T < 43$ °C	0.5; 0.25	–	[35,36]
k_B; μ_0	Boltzmann constant; vacuum permeability	1.380649 × 10^{-23}; 1.25663706212 × 10^{-6}	J K^{-1}; T m A^{-1}	[37]

Once the dose of the clinical fluid is fixed, the amount of magnetic phase no longer depends on the formulation, which is the main constraint of this study (Figure 1). The mass fraction of Fe_3O_4 varies among the six ZnO:Fe_3O_4: chitosan formulations (Figure 1a), but its mass concentration stays at 43.3 kg m^{-3} (Figure 1b), because the iron dose is prescribed. The formulations are illustrative modeling scenarios, not experimentally reported materials: two ZnO-to-Fe_3O_4 ratios represent a moderate and a ZnO-rich composite, and three chitosan-to-Fe_3O_4 ratios span matrices from polymer-rich to polymer-poor (Section 4.1). The three constituents have distinct roles: magnetite is the heat source, chitosan is a biocompatible matrix that immobilizes the cores [6], and ZnO nanoparticles interfere with zinc homeostasis in SH-SY5Y neuroblastoma cells [7]. The ratios were chosen to test, before synthesis, whether composition can modify heating at a fixed iron dose; the model is thus intended to support the numerical optimization and selection of formulations, whose synthesis and experimental characterization are planned as future work.

Composition has two further effects. It can affect heating only through heat transport, and this effect is small: the inorganic phases occupy at most 4.7% of the volume and, even as dispersed perfect conductors, would raise the effective conductivity by at most 15% (Figure 1d). The ZnO mass concentration exceeds the complete-dissolution limit measured in culture medium [9] by about four orders of magnitude, independently of the chitosan fraction (Figure 1c). This comparison refers to DMEM at 37 °C and does not establish zinc release, dissolution kinetics or bioavailability in tissue; the oxide is therefore treated as a solubility-limited reservoir, and zinc release is not modeled. The four panels separate a fixed magnetic source from a composition-dependent zinc reservoir; thermally, the six formulations are reduced to one heat source.

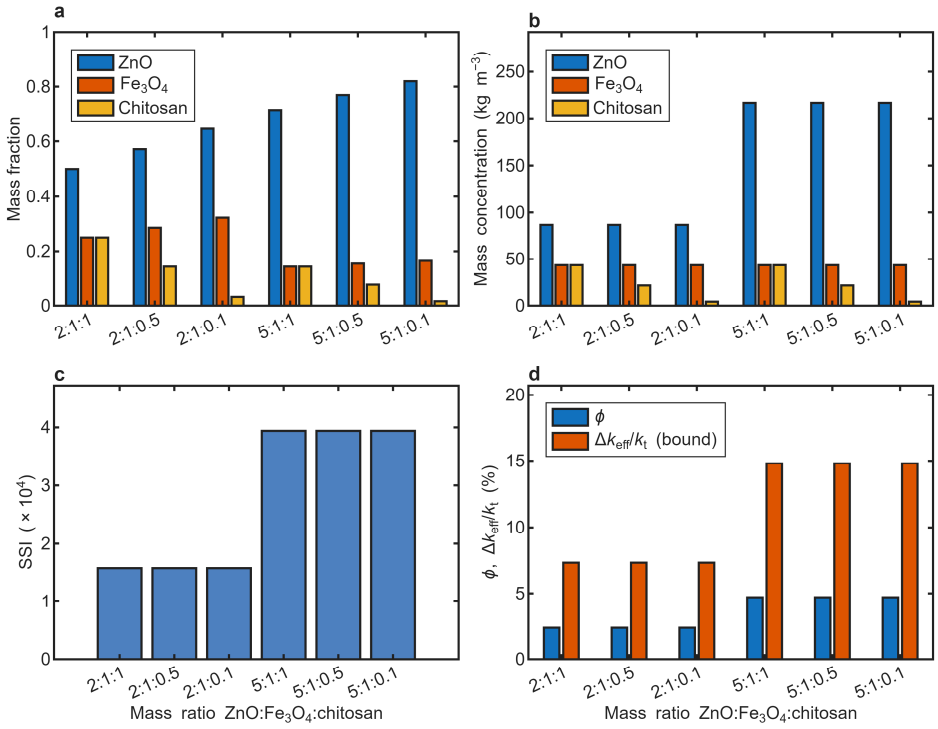


Figure 1. Six ZnO: Fe_3O_4: chitosan formulations at the clinical iron dose. (**a**) Mass fractions; (**b**) tumor-average mass concentrations, with Fe_3O_4, the heat source, fixed at 43.3 kg $m^{-3;}$ (**c**) ZnO saturation index in DMEM ($\times 10^4$); (**d**) inorganic volume fraction φ and Maxwell–Garnett bound of the conductivity increase.

2.2. Dynamic-Hysteresis Loss Beyond Linear Response

In the chitosan matrix, the loss of the three documented cores is controlled by Néel relaxation, and, for all of them, τ_N remains below $1/(2\pi f)$ (Figure 2a): the moments relax within each cycle, and only the fraction that lags behind the field dissipates energy. The 15.3 nm cores relax most slowly, because the barrier grows with core volume; the 8.1 and 10.2 nm cores respond almost linearly and heat little at 15 kA m^{-1} (Figure 2b). At H_{AB}, the SAR of the 15.3 nm cores is 4.2 W g^{-1}; at higher amplitudes, it increases subquadratically, because the field lowers the barrier without removing it (Figure 2c). Because ξ reaches unity below H_{AB}, LRT fails in this regime; relative to the two-level result, LRT overestimates the SAR by 63% at the AB limit.

The lower bound of τ_0 [25] makes the magnetization nearly reversible and lowers the SAR a hundredfold (Figure 2c), whereas a log-normal distribution built from the TEM data of [15] triples it, because the larger cores lie close to the loss maximum. The monodisperse prediction is 31% lower than the SAR reported for the fluid characterized with the clinical applicator [33], a value taken from the secondary source [34] (star). The cores of that fluid differ from the modeled ones in size, anisotropy, state (aqueous suspension) and formulation (aminosilane shell, high iron concentration). Because τ_N depends exponentially on $K_{eff}D^3$, small differences shift $2\pi f\tau_N$ and hence the loss; the gap therefore reflects the sensitivity of SAR to core properties rather than a model error. Along the AB line, the SAR barely changes up to 1 MHz, whereas along the HD line [31,32] it rises more than tenfold (Figure 2d); within the AB limit, the heat source is set by core size and τ_0, not by frequency.

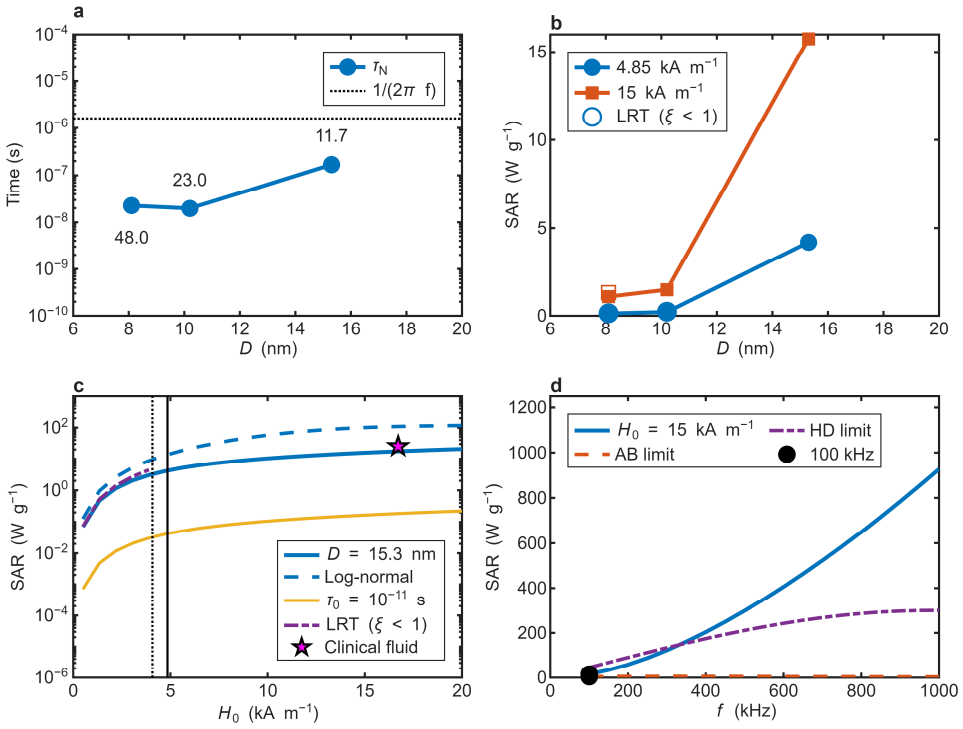


Figure 2. Magnetic loss of immobilized magnetite cores at 37 °C and 100 kHz (SAR per gram of Fe_3O_4). (**a**) Néel relaxation time of three documented (D, K_{eff}) pairs (labels: K_{eff}, kJ m^{-3}) and $1/(2\pi f)$. (**b**) Two-level SAR at H_{AB} and 15 kA m^{-1}; open symbols, LRT ($\xi < 1$). (**c**) SAR of the 15.3 nm cores versus H_0: monodisperse, log-normal TEM distribution [15], lower bound of τ_0 [25], LRT ($\xi < 1$) and fluid characterized with the clinical applicator [33], as given in [34] (star, converted to mass of Fe_3O_4); dotted line, $\xi = 1$; solid line, H_{AB}. (**d**) SAR versus frequency at 15 kA m^{-1} and along the AB and HD criteria; dot, 100 kHz.

2.3. Perfusion-Limited Heating Kinetics

Because the heat source is identical for all composition ratios, the thermal response is practically the same. Figures 3–5 therefore compare six cases: two CNS NB-FOXR2 volumes, 115 mL (the cohort mean) and 10.5 mL (the second-smallest lesion, chosen so that the small case is not set by a single extreme value) [23], each at three amplitudes (2, 4.85 and 15 kA m^{-1}). The two volumes bracket the two thermal regimes, $R_t/L_t \approx 6$ and 2.7 (Equation (7)), and intermediate sizes fall between them; the 115 mL case requires more fluid than was injected clinically (Section 4.1) and is a hypothetical computational scenario.

Heating is fast compared with the 60 min session and is limited by perfusion (Figure 3). The initial rise is nearly adiabatic and set by the heat source; within minutes, all the curves reach a plateau. At the AB field, the center of the larger volume stabilizes at 44.0 °C, whereas that of the smaller volume saturates at 42.7 °C, because more heat diffuses into the host (Figure 3a); near H_{AB}, volume therefore decides whether the center exceeds 43 °C. The four panels follow one energy balance at increasing distance from the center. In the larger case, the rise at the edge is about half that at the center (Figure 3c), as expected for a homogeneous source (Equation (7)); two centimeters outside the boundary, it stays below 0.2 K (Figure 3d), consistent with the treatment-planning aim of [1] that 43 °C should not be exceeded beyond 2 cm from the tumor. After switch-off, the central excess halves within about 2 min, consistent with the perfusion-limited half-life $t_{1/2} = \ln(2)\rho c_p/(\omega C_b)$; the decay is faster in the smaller case, where conduction into the host adds a second cooling path. Perfusion thus controls both the plateau and the cooling.

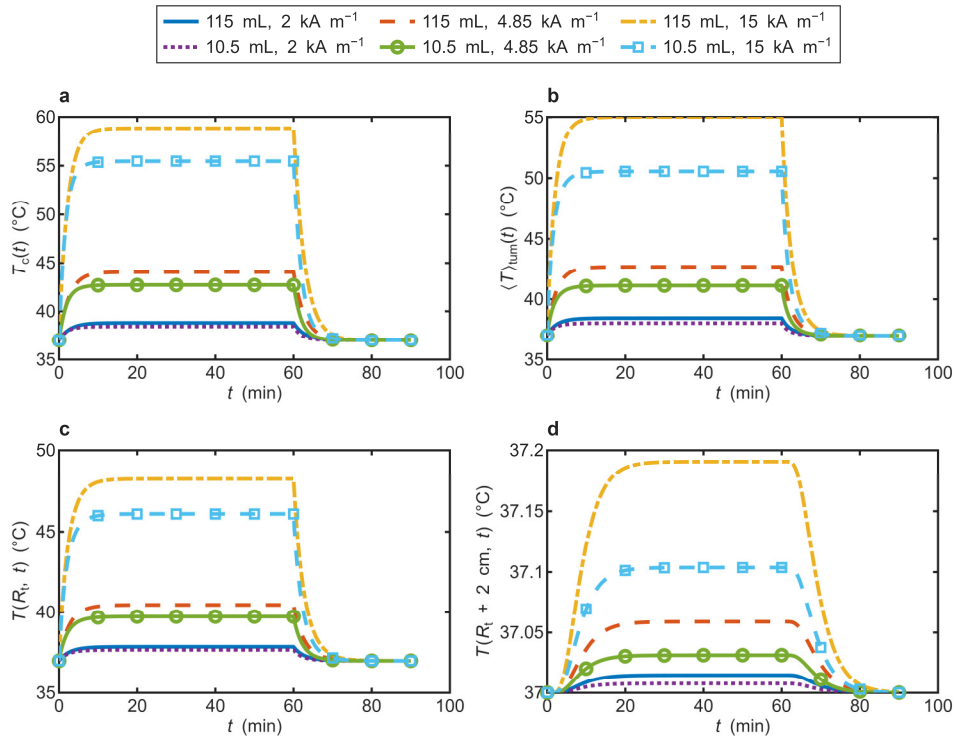


Figure 3. Heating kinetics of the six cases (practically identical for all mass ratios) during 60 min of heating and 30 min of cooling. (**a**) Center, T_c; (**b**) volume mean $\langle T \rangle_{tum}$; (**c**) edge, $T(R_t)$; (**d**) 2 cm beyond the edge. The amplitude 4.85 kA^{-1} m^1 is H_{AB}.

Lesion size shapes the radial temperature profile (Figure 4). At 1 min, the central values of the two volumes nearly coincide at each amplitude (Figure 4a), because the early rise is set only by the local source and the heat capacity. At 5 min, the profile of the 115 mL case has flattened over most of the radius, whereas the 10.5 mL case still shows a conduction-dominated profile (Figure 4b). At 15 and 60 min, the profiles hardly change (Figure 4c,d), so the steady state is reached long before the end of heating. The steepest gradients occur at the interface, where the source ends and the host removes the heat; there, the rise decays over a few millimeters, the scale of the perfusion length.

The difference between the two volumes is set by the ratio of the radius to the perfusion length, R_t/L_t, with $L_t \approx 5$ mm. For $R_t \gg L_t$, the steady rise approaches the perfusion-limited value $q/(\omega C_b)$, independently of size. With $R_t \approx 6L_t$, the center of the larger case almost reaches this value, whereas the smaller case attains only part of it, because heat is conducted into the host (Equation (7)). Figures 3 and 4 describe the same balance in time and in space: the plateaus of Figure 3 correspond to the flat cores of the profiles, and the faster cooling of the small case reflects its larger surface-to-volume ratio. Because the SAR is evaluated at the local temperature, the plateaus and profiles already include the slight decrease in the loss as the cores heat (Section 4.2). The minimum local SAR needed for a given center temperature follows from this energy balance alone, independently of the magnetization model (Section 4.5), so the magnetic and thermal parts of the problem can be checked separately.

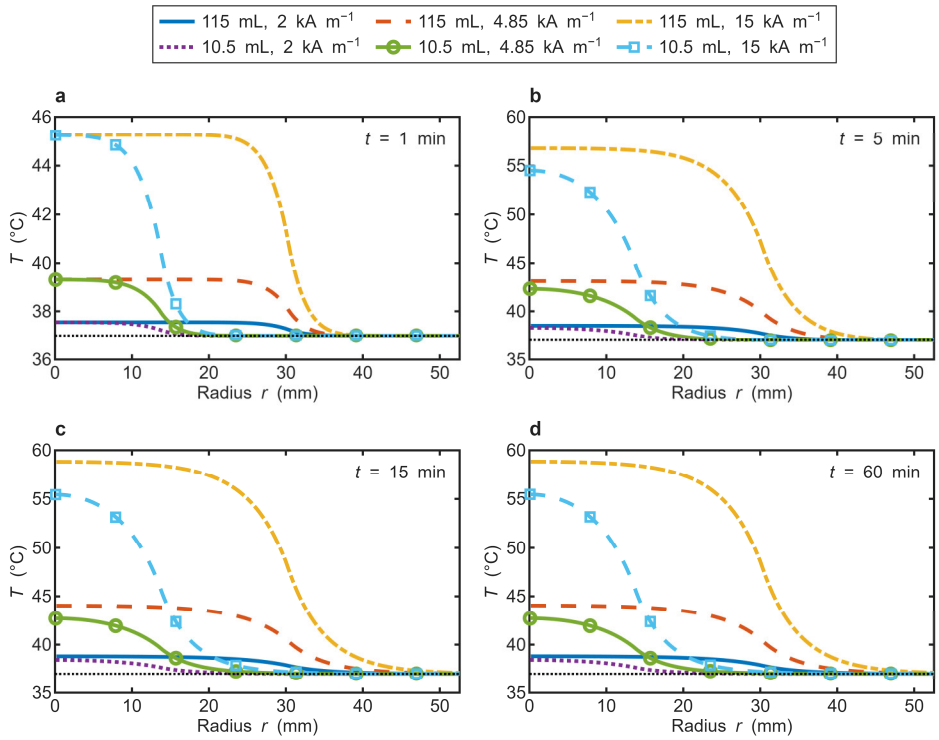


Figure 4. Radial temperature profiles of the six cases. (**a**) 1 min, (**b**) 5 min, (**c**) 15 min and (**d**) 60 min (end of heating), for the 115 and 10.5 mL cases at 2, 4.85 (H_{AB}) and 15 kA m^{-1}; line styles as in Figure 3; tumor edges at R_t = 30.2 mm (115 mL) and 13.6 mm (10.5 mL); dotted line, T_a.

2.4. Thermal Dose

Converted into CEM43, the computed thermal histories show that small differences in temperature produce large differences in thermal dose (Figure 5). Over the applicator range, the central CEM43 of the larger volume spans about seven orders of magnitude (Figure 5a), whereas its central temperature changes by about 20 K (Figure 3a). The reason is the exponential form of Equation (6): each degree above 43 °C doubles the dose rate, and each degree below it reduces the rate fourfold. The dose therefore accumulates mainly during the plateau, at a nearly constant rate, and the 30 min of cooling add little. At every amplitude, the dose of the smaller volume lags behind, because its plateau is lower; at 2 kA m^{-1}, neither volume accumulates more than a fraction of an equivalent minute.

Coverage shows the consequence (Figure 5b). The AB field is the most sensitive case: the two central plateaus lie on opposite sides of 43 °C; therefore, 30 equivalent minutes are reached in 59% of the larger volume but in only 2% of the smaller one. At 15 kA m^{-1}, by contrast, both volumes are fully covered within minutes. Panels c and d give the spatial counterpart. Between the center and one host perfusion length beyond the boundary, CEM43 falls by several orders of magnitude (Figure 5c); the far-field plateau is the negligible baseline of Equation (6) after 90 min at 37 °C. In all six cases, the volume mean stays within about one order of magnitude of the central value, whereas the peritumoral shell receives much less (Figure 5d). Coverage is therefore decided at the tumor edge, not at the center, and near H_{AB} it behaves as a threshold in amplitude rather than as a gradual function.

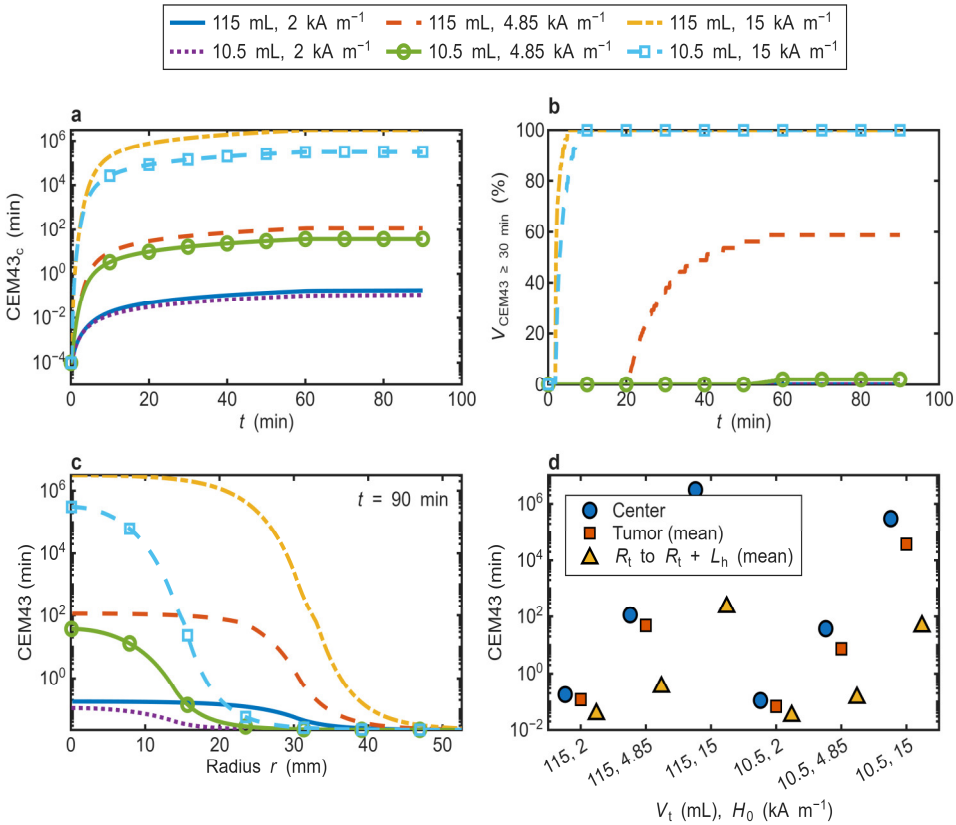


Figure 5. CEM43 thermal dose of the six cases (line styles as in Figure 3). (**a**) Center versus time; (**b**) volume fraction with CEM43 ≥ 30 min; (**c**) radial profile at 90 min; (**d**) center, volume mean and peritumoral shell (R_t to $R_t + L_h$, with L_h the host perfusion length) at 90 min, labeled by volume (mL) and amplitude (kA m^{-1}).

2.5. Amplitude Window for Median Temperature and Dose Coverage

Amplitude–time maps of the 115 mL case locate the temperature and dose thresholds over the applicator range (Figure 6). A median T_{50} of 43 °C requires 4.9 kA m^{-1}, practically the AB value (Figure 6a). Coverage of 90% with CEM43 ≥ 30 min requires 6.2 kA m^{-1}, and with CEM43 ≥ 240 min, 8.8 kA m^{-1} (Figure 6b,c). The difference between these thresholds comes from the radial gradient. The median is set by the nearly isothermal core, whereas 90% coverage also requires heating of the outer shell, whose rise is only about half that of the core; since the dose grows exponentially with temperature, the shell requires much higher amplitudes. Reaching 240 instead of 30 equivalent minutes requires an eightfold dose, that is, a coverage boundary a few kelvin warmer (Equation (6)).

The maps differ in their time dependence. The 43 °C contour of the median becomes horizontal within about 10 min, whereas the coverage contours descend until switch-off, because the dose integrates the thermal history; cooling afterwards adds little. Accordingly, the time needed for 90% coverage falls steeply above each threshold and reaches a few minutes at 15 kA m^{-1} (Figure 6d). The perfusion response shifts all thresholds: a collapse of tumor perfusion above 42 °C (Section 4.3) lowers the amplitudes required for T_{50} = 43 °C and for 90% coverage (dashed contours), whereas hyperthermic vasodilation [5] raises them (dotted contours). Each threshold can be traced back to the inputs of Table 1.

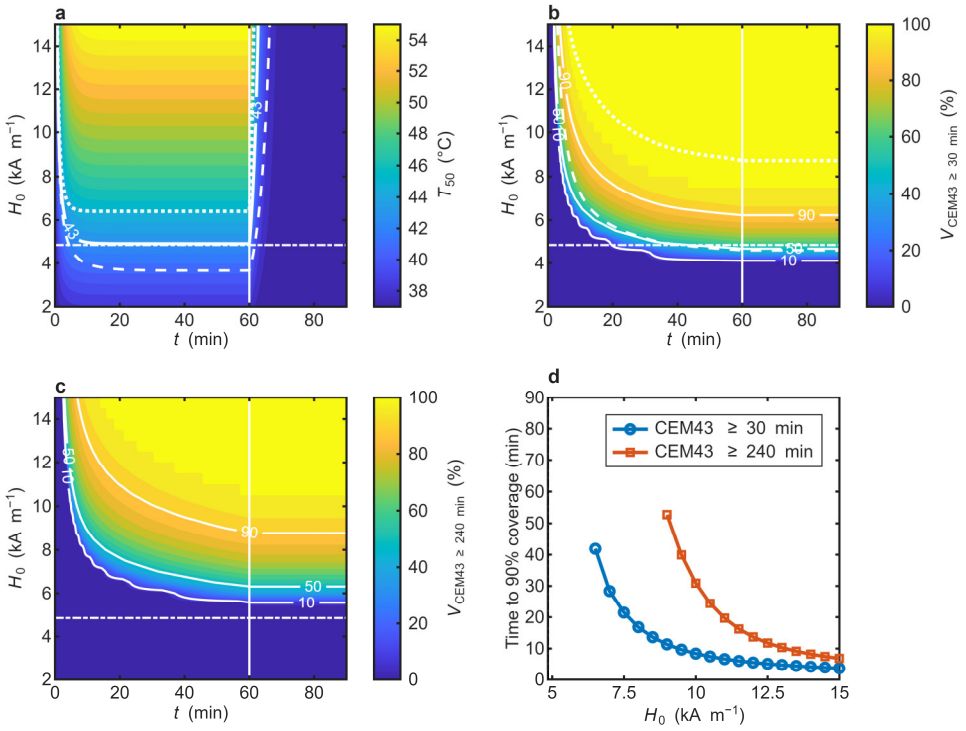


Figure 6. Amplitude–time maps for the 115 mL case. (**a**) Median T_{50}; white contour, 43 °C. (**b**,**c**) Volume fraction with CEM43 ≥ 30 min and ≥ 240 min; white contours, 10, 50 and 90%. In (**a**,**b**), 43 °C and 90% contours with collapse of tumor perfusion [38] (dashed white lines) and hyperthermic vasodilation [5] (dotted white lines). Vertical line, switch-off; dash-dotted line, H_{AB}. (**d**) Time to cover 90% of the volume, where reached within 90 min.

2.6. Exposure-Equivalent Temperatures and Spatial Coverage

On a time–temperature plane, the median doses can be read as isothermal exposures (Figure 7a). According to Equation (6), the median dose at H_{AB} is equivalent to an exposure at 43 °C for the 115 mL case and at 41 °C for the 10.5 mL case, whereas at 15 kA m^{-1} it corresponds to more than 50 °C. The two benchmark points are in vitro experiments on the SH-SY5Y cell line: 43 °C for 30 min, a non-lethal stress stimulus [39,40], and 46 °C for 30 min, at which magnetic and external heating differ most [41]. At H_{AB}, the dose of the larger volume is similar to the non-lethal exposure and the smaller volume receives less, whereas at 15 kA m^{-1} both exceed the dose of the 46 °C exposure. The comparison concerns the thermal dose only, not the biological outcome.

The spatial distribution of the dose follows from panels b–d. At the end of heating, the 41–43 °C isotherms remain inside the 115 mL volume at the AB field (Figure 7b), whereas at 15 kA m^{-1} they extend several millimeters into the host (Figure 7c). The isotherm radii grow steeply between about 3 and 6 kA m^{-1} and then saturate: the 43 °C isotherm reaches the boundary at about 8 kA m^{-1}, and beyond this amplitude its radius grows only slightly, while the white-matter volume above 41 °C keeps increasing (Figure 7d). The saturation follows from the perfusion length of the host, which limits how far heat penetrates beyond the boundary. The figure thus links the dose equivalents of panel a to their spatial extent and shows that, above about 8 kA m^{-1}, a higher amplitude adds little coverage and mainly heats the adjacent white matter.

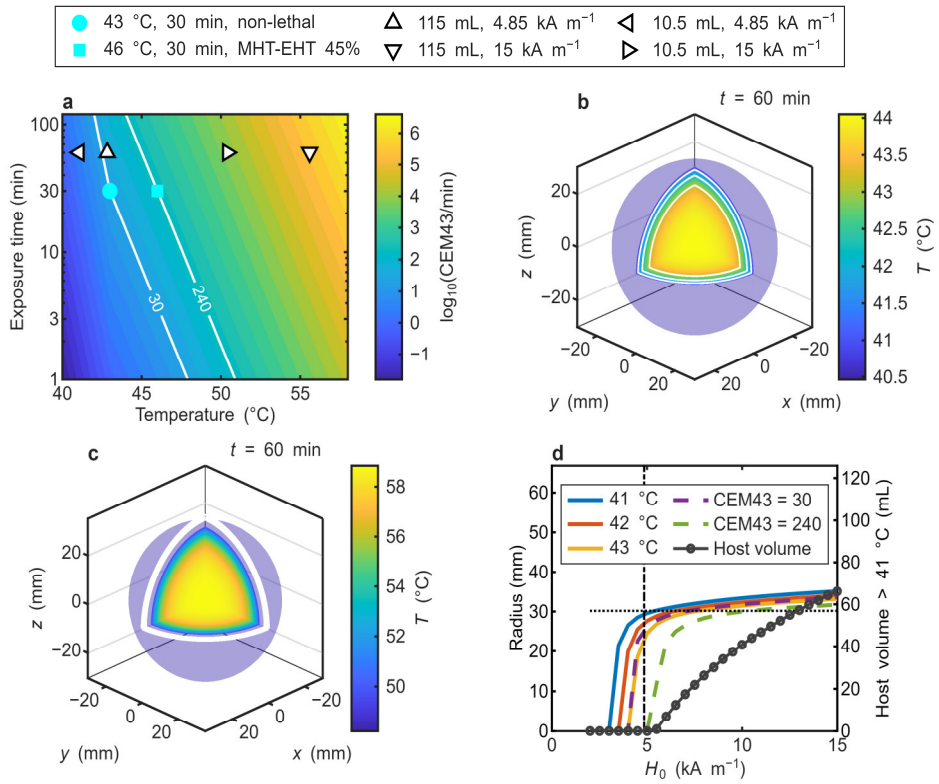


Figure 7. Dose equivalents. (**a**) CEM43 of isothermal exposures; circle and square, S-SY5Y benchmarks [39–41]; triangles, median doses of four cases as 60 min equivalents. (**b**,**c**) 115 mL case at 4.85 and 15 kA m^{-1} at the end of heating (t = 60 min); white arcs, 41–43 °C isotherms. (**d**) Radii of the 41–43 °C isotherms at 60 min and of the CEM43 = 30 and 240 min surfaces at 90 min (left axis), and white-matter volume above 41 °C at steady state (right axis); dotted line, Rt; dash-dotted line, HAB.

2.7. Numerical Verification

The numerical solution is verified in the upper row of Figure 8. Changing the integration time step or the number of easy-axis orientations alters the SAR by less than 0.2% (Figure 8a); changing the grid resolution or the extent of the host domain alters five thermal and dose metrics by less than 0.1% (Figure 8b); and the energy balance closes to rounding error (Figure 8c). The ratio of the two-level to the LRT loss falls from about 1 at small ξ to 0.2 at the maximum amplitude (Figure 8d), so LRT remains accurate only for ξ well below unity. These checks establish numerical stability, not predictive accuracy, which is limited by the uncertainty of the physical inputs.

2.8. Physical-Parameter Uncertainty

The lower row of Figure 8 quantifies this limitation. The collapse of tumor perfusion above 42 °C raises the median temperature, and vasodilation lowers it (Figure 8e). When all literature-bounded inputs are sampled together (Section 4.6), T50 at HAB at the end of heating has a median of 44 °C and a 5th–95th percentile range of 37–59 °C; the lower edge of the band stays below 43 °C over the whole applicator range. The total Sobol indices (Figure 8f) identify the width of the size distribution (0.71) and $\tau 0$ (0.26) as the dominant inputs, followed by tumor perfusion, whereas Keff and host perfusion contribute little; the first-order indices are only slightly lower, so interactions between the inputs are weak. The uncertainty of the predictions is therefore magnetic rather than numerical, and the deterministic curves of Figures 3–7 should be read together with these intervals.

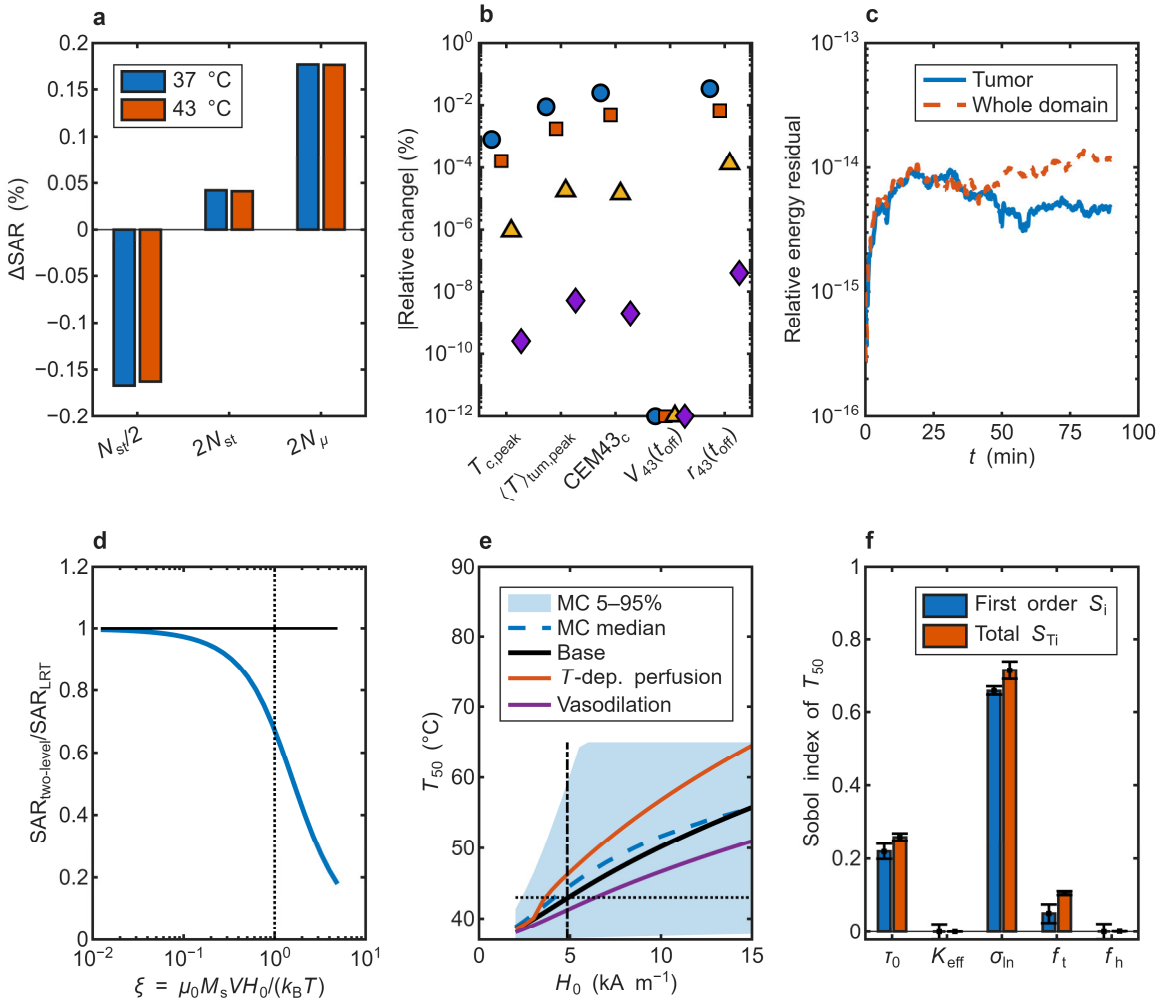


Figure 8. Numerical verification (**a**–**d**) and parameter uncertainty (**e**,**f**); 115 mL case at H_{AB} unless stated. (**a**) SAR change at 15 kA m^{-1} for halved or doubled integrator steps (N_{st}) and doubled easy-axis cones (N_{μ}). (**b**) Change of five output metrics for 40 and 80 radial cells (circles, squares; relative to 160) and host thicknesses of 6 and 10 perfusion lengths (triangles, diamonds; relative to 14); markers on the lower axis, no change. (**c**) Energy-balance residual. (**d**) Two-level to LRT loss ratio versus ξ. (**e**) T_{50} versus H_0 with temperature-dependent tumor perfusion [38], vasodilation [5], and Monte Carlo median and 5th–95th percentile band. (**f**) Sobol indices of T_{50}.

3. Discussion

The chain from literature inputs to heat source and temperature is fully traceable, which allows us to ask whether such a model can describe the thermal-dose response without losing the provenance of any input. First, at a fixed clinical iron dose, the composition does not alter the magnetic heat source; it changes the median rise by at most 1.3%, and only through the thermal conductivity. The composition can therefore be chosen on non-thermal grounds: for the planned synthesis, the model fixes the magnetite dose by the heating requirement and leaves the ZnO and chitosan fractions to be optimized for zinc release and matrix properties. This choice is nevertheless constrained: for the 115 mL case and ZnO:Fe_3O_4 = 5, the tumor would contain about 25 g of ZnO, far more than can dissolve at the solubility limit measured in culture medium [9]. If zinc delivery is intended, lower ZnO-to-Fe_3O_4 ratios or direct measurements in tissue-relevant environments are needed. Two model findings are relatively insensitive to the specific parameter set: (i) LRT becomes invalid above about 4 kA m^{-1} at 100 kHz, consistent with dynamic-hysteresis [11] and kinetic Monte Carlo calculations [14]; relative to the two-level result, LRT would

therefore overestimate the heat source by 63% at the AB field, and the subquadratic dependence on H_0 agrees qualitatively with the saturation of the SAR observed experimentally [16]. (ii) In tumors with a radius above about five perfusion lengths, the central rise is set mainly by the ratio of the heat source to perfusion; for the assumed dose and perfusion, reaching 43 °C therefore requires a local SAR of at least 3.1 W g^{-1} for any uniform source (Section 4.5). The smaller lesion is conduction-limited and needs 6.6 kA m^{-1} for T_{50} = 43 °C; according to Equation (7), intermediate volumes fall between the two cases.

The therapeutic window is narrow: T_{50} reaches 43 °C at an amplitude only about 1% above the AB value, whereas 90% coverage with CEM43 ≥ 30 min requires an amplitude about 28% higher. The AB condition was introduced as an exposure limit [30], but an in vivo study in rats regards it as conservative [32]. Above the AB field, the gain in coverage must be weighed against heating of the adjacent white matter (Figure 7d). Up to about 5 kA m^{-1}, no host tissue exceeds 41 °C; at the 6.2 kA m^{-1} needed for 90% coverage, about 9 mL of white matter exceeds it. Above about 8 kA m^{-1}, the 43 °C isotherm has reached the tumor edge, so a further increase in amplitude adds little coverage and mainly heats the host. For the 115 mL case, the useful amplitude is therefore limited to about 6–8 kA m^{-1}. The upper limit of the applicator, 15 kA m^{-1} at 100 kHz, corresponds to $H_0 f = 1.5 \times 10^9$ A m^{-1} s^{-1}, three times the AB value and 30% of the HD criterion [31,32]. Near this limit, eddy currents add a non-specific source that is not included in the model. For a conductor of electrical conductivity σ_{el}, the induced power density is $\sigma_{el}(\pi f \mu_0 H_0 r)^2/2$, with r being the distance from the axis of the applied field. The conductivity of cerebrospinal fluid at 37 °C, measured between 10 Hz and 10 kHz without systematic frequency dependence [42], exceeds the low-frequency values of gray and white matter [43]. If this value is assumed to hold at 100 kHz and is taken as an upper bound for intracranial tissue, the perfusion-limited rise of the white matter at r = 5 cm is about 0.5 K at H_{AB} and about 5 K at the upper limit. Because the power density grows as r^2, the AB criterion, derived for the human trunk, is conservative for the smaller cross-section of a child's head, consistent with the HD criterion for smaller body regions [31,32]. Results above about 8 kA m^{-1} should therefore be regarded as high-amplitude scenarios that require coupled electromagnetic–thermal modeling of the head [22].

All results refer to the composite case study of Table 1, assembled from independent sources [1,5,15,23,27]. The model has not been validated against clinical thermometry, which was performed under heterogeneous nanoparticle deposition [1], a condition that substantially alters the heating pattern [21]. For the 115 mL case, applying the median dose ratio implies a total injected fluid volume about three times the maximum volume administered to patients [1]; these results are therefore a hypothetical computational scenario rather than a clinical protocol. For monodisperse cores, the largest single uncertainty comes from the reported range of the Néel attempt time τ_0 [25,44]. Below the loss maximum, the loss is nearly proportional to τ_N, so the lower bound of τ_0 can reduce it by up to two orders of magnitude. With a log-normal distribution constructed from the TEM size spread reported in [15], the loss is about three times larger and much less sensitive to τ_0 (−34% at its lower bound), because part of the magnetite mass always lies near the loss maximum. A monodisperse model would therefore overestimate the loss only if the mean size lay at the loss maximum; here, the mean size lies below it, and the monodisperse loss is a lower estimate. Accordingly, the Sobol analysis attributes most of the variance of T_{50} to the size distribution and τ_0 (Figure 8f). Because K_{eff} was extracted in [15] with a single core size, a consistent treatment requires a joint fit of K_{eff}, τ_0 and the size distribution. The SAR reported for the fluid characterized with the clinical applicator [33,34], which lies between the monodisperse and polydisperse predictions (Figure 2c), illustrates the width of this uncertainty. AC susceptibility and AC magnetometry measurements over 10–500 kHz on an immobilized formulation, planned as future experimental work, could provide

these parameters and turn this dominant uncertainty into an experimentally constrained one.

Further limitations follow from the model assumptions. (i) Interactions. The cores are treated as non-interacting, consistent with the K_{eff} determined at infinite interparticle separation [15]; an apparent, interaction-affected value would count the interactions twice. At the tumor-average loading (0.84 vol%), the mean core spacing is about four diameters and the dipolar energy $\mu_0 m^2/(4\pi d^3)$ shifts τ_N by less than 10%, an effect comparable to that of the second K_{eff} value [15]. Aggregation within cells raises the local loading and can increase or decrease the loss [14,17,45]; this regime requires interacting kinetic Monte Carlo models and is not included. (ii) Brownian rotation. For a freely rotating 15.3 nm core in water at 37 °C, the Brownian time $3\eta V_H/k_B T$, computed with the viscosity of water [46], is at least about 0.9 μs, comparable to $1/(2\pi f)$, so Brownian loss could contribute in a free suspension. In the chitosan network, a core can only twist elastically rather than rotate freely; steady Brownian dissipation at 100 kHz is therefore suppressed, and Néel relaxation remains the only loss mechanism, consistent with the reduced loss measured after immobilization or cell uptake [16,17]. Partial alignment of the easy axes, for example in a gel formed in a field, would enlarge the hysteresis loop [11] and, for full alignment, raise the SAR about threefold; the random-axis, fully immobilized case is therefore a conservative estimate of the source. For random and aligned easy axes alike, the two-level model does not rely on LRT.

(iii) Continuum perfusion. The Pennes term averages perfusion over volumes larger than the vessel spacing and cannot represent discrete large vessels, microvascular proliferation, necrosis or shunts. Hot spots around particle clusters are nevertheless negligible: by our estimate, a cluster of pure magnetite with a radius of 100 μm, heated at the SAR of the AB limit, raises its center by only about 0.2 K above its surroundings. This is consistent with the conclusion of [47] that hyperthermia requires a nanoparticle-loaded region at least 1 mm in diameter. Local gradients therefore arise on the millimeter scale of the deposits; the grid, which is much finer than the perfusion lengths, resolves this scale, but the distribution of the deposits, which controls the heating pattern [21,22], is not known. Discrete-vessel or image-based models, as used for heterogeneous deposits [21,22], are the natural next step once imaging data of the vasculature and of the particle distribution become available. Necrosis and shunts change the local perfusion; this uncertainty is bounded by the perfusion range sampled in Section 4.6.

(iv) Geometry and properties. A sphere has the smallest surface-to-volume ratio, and uniform deposition gives the smoothest profile. An irregular lesion of the same volume loses more heat through its boundary, and heterogeneous deposition creates hot and cold regions [1,21], which raise the peak temperature; both effects reduce the coverage at a given mean iron dose, because the under-dosed regions control the 90% coverage. Piecewise-constant properties impose a sharp tumor–host interface, whereas the infiltrative margin of CNS NB-FOXR2 [23] would smooth the edge gradient. The effects of perfusion collapse and vasodilation are shown in Figures 6 and 8e; the temperature dependence of conductivity changes the steady median rise by only 0.1%, and a gray-matter host lowers it by about 5%. Since M_s and K_{eff} are kept constant, thermal activation is the only source of the temperature dependence of SAR and lowers it by about 10% between 37 and 43 °C, whereas measured SAR can also change through these properties [18]. Chitosan and gel water are treated as part of the tissue phase, although the effective conductivity of magnetic composites depends on their porosity and topology [48]. In addition, cerebrospinal fluid [5] is not included; the lesion conductivity is based not on CNS NB-FOXR2 tumor tissue but on measurements on neuroblastoma cells [27]; the tissue properties are proxies taken from another pediatric brain tumor [5]; and the single-patient relative blood flow [28] serves only as an independent consistency check. Because CEM43 ignores

sensitization and heat-induced perfusion changes [49], the thresholds of 30 and 240 min serve only as thermal-dose indicators, not as evidence of cell death or treatment efficacy.

4. Methods

All calculations are performed using a standalone MATLAB R2019a script, without any fitting parameters; no new experimental data were generated, and all measured quantities were taken from the cited literature. Each physical input is read from a fixed reference database that stores its value, unit and provenance; the calculation stops whenever the provenance is missing or an input differs from the stored value. The calculation proceeds in six stages (Sections 4.1–4.6): (i) average composition at the clinical iron dose; (ii) magnetic loss of immobilized cores using a two-level dynamic hysteresis model [11]; (iii) solution of the Pennes bioheat equation for a sphere embedded in white matter [19] using a finite-volume method with implicit time stepping; (iv) calculation of the CEM43 thermal dose metric [35,36]; (v) an analytical solution of the steady-state problem used to interpret the numerical results; and (vi) a literature-bounded uncertainty and sensitivity analysis. Numerical checks are reported in Section 2.7 and the uncertainty analysis in Section 2.8; all symbols are defined in Table 2.

Table 2. Mathematical notation.

Symbol	Definition	Unit
E, θ, ψ	Magnetic energy of a core; angle of the moment to the easy axis; angle of the easy axis to the field	J; rad; rad
V, D	Core volume ($\pi D^3/6$) and diameter	m^3; m
K_{eff}	Effective uniaxial anisotropy constant	J m^{-3}
$H(t)$, H_0, f	Applied field, its amplitude and frequency	A m^{-1}; A m^{-1}; Hz
h, H_K	Reduced field H/H_K; anisotropy field	–; A m^{-1}
μ_0, k_B	Vacuum permeability; Boltzmann constant	T m A^{-1}; J K^{-1}
M_s	Saturation magnetization	A m^{-1}
n_1, n_2	Occupation probabilities of wells 1 ($\cos\theta > 0$) and 2 ($\cos\theta < 0$), $n_2 = 1 - n_1$	–
ν_1, ν_2	Escape rates from wells 1 and 2	s^{-1}
Δe_1, Δe_2	Barriers of wells 1 and 2 in units of $K_{eff}V$	–
σ	Reduced barrier $K_{eff}V/k_BT$	–
τ_0, τ_N	Néel attempt time; Néel relaxation time $\tau_0 e^{\sigma}$	s
p_1, p_2	Field projection of the moment in wells 1 and 2	–
M_ψ	Magnetization along the field for easy-axis angle ψ	A m^{-1}
$W(\psi)$	Hysteresis loss per cycle and per unit volume of magnetite	J m^{-3}
$\langle\cdot\rangle_\psi$, N_μ	Average over easy-axis orientations; number of orientation cones	–; –
SAR, SAR_{LRT}	Specific absorption rate per unit mass of Fe_3O_4 (two-level model; LRT), reported in W g^{-1}	W kg^{-1}
ρ_{Fe3O4}	Density of magnetite	kg m^{-3}
χ_0, ξ	Equilibrium susceptibility; ratio of Zeeman to thermal energy	–; –
T, T_a	Temperature, in K in σ, τ_N, χ_0 and ξ (Equations (2)–(4)) and in °C in Equations (5)–(7); arterial temperature	K; °C
r, t, s	Radial coordinate; time; integration variable	m; s; s
ρ, c_p, k	Tissue density, specific heat and thermal conductivity	kg m^{-3}; J kg^{-1} K^{-1}; W m^{-1} K^{-1}
ωC_b	Perfusion coefficient	W m^{-3} K^{-1}
q	Volumetric heat source	W m^{-3}
c_{Fe3O4}	Tumor-average Fe_3O_4 concentration	kg m^{-3}
R_t, t_{on}	Tumor radius; heating time	m; s

CEM43, $CEM43_{50}$	Cumulative equivalent minutes at 43 °C; median value (50% of the volume)	min
R, R_{eq}	CEM43 base	–
T_{eq}	Constant temperature giving $CEM43_{50}$ in 60 min	°C
k_t, k_h; L_t, L_h	Conductivity and perfusion length $(k/\omega C_b)^{1/2}$ of tumor and host	W m^{-1} K^{-1}; m
x, y, Λ	R_t/L_t; R_t/L_h; denominator in Equation (7)	–
T_{thr}, SAR_{req}	Target center temperature; minimum local SAR to reach it	°C; W kg^{-1}
σ_{ln}	Width of the log-normal size distribution (standard deviation of ln D)	–
σ_{el}	Electrical conductivity of tissue (eddy-current estimate)	S m^{-1}
$(\omega C_b)_t(T)$, $k(T)$	Temperature-dependent tumor perfusion coefficient and conductivity (sensitivity cases)	W m^{-3} K^{-1}; W m^{-1} K^{-1}
S_i, S_{Ti}	First-order and total Sobol indices of T_{50}	–

4.1. Composition at the Clinical Iron Dose

The iron concentration $c_{Fe,fl}$ = 112 kg m^{-3} refers to the administered clinical fluid, not to tissue. With the median dose d = 0.28 mL of fluid per cm^3 of tumor [1], the average iron concentration in the treated volume is $c_{Fe,fl}d$ = 31.4 kg m^{-3}. Assuming that all iron is present as Fe_3O_4 (for maghemite, the conversion factor would be 3.5% larger) and using standard atomic weights [50], $c_{Fe3O4} = c_{Fe,fl}\, d\, M_{Fe3O4}/(3M_{Fe})$ = 43.3 kg m^{-3} is obtained for each composite formulation. The conversion also assumes a uniform distribution of the fluid and no particle loss during treatment. Applying this median dose ratio, the 115 mL case requires 32.2 mL of fluid, 2.8 times the largest volume injected in the clinical trial (11.6 mL) [1], whereas the 10.5 mL case requires 2.9 mL; the larger case is therefore a hypothetical computational scenario. It would also contain 5.0 g of Fe_3O_4 together with 10.0 g of ZnO at the lower ratio or 24.9 g at the higher ratio. The zinc oxide and chitosan contents were defined by the mass ratios $r_Z = c_{ZnO}/c_{Fe3O4}$ and $r_C = c_{chitosan}/c_{Fe3O4}$, with $r_Z \in \{2, 5\}$ and $r_C \in \{1, 0.5, 0.1\}$; these are illustrative design scenarios, not experimentally reported formulations. The volume fraction of the inorganic components, $\varphi = c_{ZnO}/\rho_{ZnO} + c_{Fe3O4}/\rho_{Fe3O4}$, using ρ_{ZnO} = 5606 kg m^{-3} [51], is 0.84% for magnetite alone. It is used to estimate the upper limit of the relative effective thermal conductivity through the Maxwell–Garnett relation, $k_{eff}/k_t \le (1 + 2\varphi)/(1 - \varphi)$, for dispersed spherical inclusions in the limit of infinite conductivity and no interfacial resistance [52]. This limit coincides with the Hashin–Shtrikman lower bound for a continuous biological-tissue matrix [52,53], while percolating inclusion networks may exceed the Maxwell–Garnett estimate. The zinc oxide saturation index is defined as the ZnO mass concentration normalized to the complete-dissolution limit of 5.5 µg mL^{-1} measured in DMEM at 37 °C [9].

4.2. Magnetic Loss

Each core is treated as a Stoner–Wohlfarth particle [12], a single-domain particle with uniaxial anisotropy whose moment rotates coherently. The easy axis forms an angle ψ with the external magnetic field, while the magnetic moment makes an angle θ with the easy axis. The reduced energy is

$$\frac{E(\theta;\psi,t)}{K_{\mathrm{eff}}V} = \sin^2\theta - 2h(t)\cos(\theta-\psi), \qquad h(t) = \frac{H(t)}{H_K}, \qquad H_K = \frac{2K_{eff}}{\mu_0 M_s}, \qquad H(t) = H_0 \sin(2\pi f t) \tag{1}$$

For every (h, ψ), the minima θ_1 (cos $\theta > 0$) and θ_2 (cos $\theta < 0$), together with the lowest saddle point, yield the reduced barrier heights Δe_1 and Δe_2 and the field projections p_i = cos($\theta_i - \psi$). If one minimum vanishes, the magnetic moment switches to the surviving

well. Within the two-level approximation [11], the occupation probabilities of wells 1 and 2, n_1 and $n_2 = 1 - n_1$, obey the master equation ($dn_2/dt = -dn_1/dt$)

$$\frac{dn_1}{dt} = \nu_2\,(1 - n_1) - \nu_1\,n_1, \qquad \nu_i = \frac{1}{2\tau_0}\,exp(-\sigma\,\Delta e_i),$$
$$\sigma = \frac{K_{eff}V}{k_B T}, \qquad n_1\left(t + \frac{1}{f}\right) = n_1(t) \tag{2}$$

When $h = 0$, both reduced barrier heights are unity, and the relaxation time $(\nu_1 + \nu_2)^{-1}$ reduces to $\tau_N = \tau_0 \exp(\sigma)$, where τ_N is the Néel relaxation time [13,44]. The two-level description rests on a separation of time scales. Within a well, the moment relaxes on the precession time $1/(\gamma\mu_0 H_K) \approx 0.1$ ns (γ, gyromagnetic ratio of the electron [37]; $\mu_0 H_K = 2K_{eff}/M_s \approx 52$ mT), much faster than the Néel time $\tau_N \approx 0.17$ µs, which is in turn shorter than the field period $1/f = 10$ µs. The moments therefore occupy the instantaneous energy minima, and the magnetization is determined by the occupations of the two wells. Since $h = H_0/H_K \leq 0.36$ remains below the minimum Stoner–Wohlfarth switching field ($h = 0.5$ at $\psi = 45°$), neither well disappears during the cycle, and reversal is purely thermally activated. Transient cycles are eliminated by imposing the time-periodicity condition in Equation (2), so that the solution directly represents the steady periodic state. The periodic start $n_1(0)$ follows in closed form from the one-cycle propagator of the exponential integrator described below. The cores are immobilized (no Brownian rotation), do not interact with each other, and their easy-axis orientations are random (uniformly distributed in $\cos\psi$). The non-equilibrium magnetization along the field and the energy dissipated per cycle and unit volume are

$$M_\psi(t) = M_s[n_1 p_1 + (1 - n_1)\,p_2], \qquad W(\psi) = -\mu_0 \oint M_\psi\,dH,$$
$$SAR = \frac{f}{\rho_{Fe_3O_4}}\,\langle W\rangle_\psi = \frac{f}{\rho_{Fe_3O_4}}\int_0^1 W\,(\psi)\,d(cos\,\psi) \tag{3}$$

Here, $W(\psi) = \mu_0 \oint H\,dM_\psi = -\mu_0 \oint M_\psi\,dH$ is evaluated using the trapezoidal rule over the N_{st} steps of the periodic solution, and $\langle W\rangle_\psi$ is the loss per cycle. The orientation average is carried out over $N_\mu = 16$ cones defined by $\cos\psi_j = (j - 1/2)/N_\mu$, yielding $\langle W\rangle_\psi = N_\mu^{-1}\Sigma_j W(\psi_j)$. Owing to symmetry, the interval $0 \leq \cos\psi \leq 1$ is sufficient to represent the full orientation distribution. The SAR is normalized per unit mass of Fe_3O_4 and depends on H_0, f, and, through σ and ν_i, also on T. For a log-normal distribution of core diameters of width σ_{ln} [10,15,24], each size contributes in proportion to its magnetite mass, so the SAR is averaged with mass weights, $SAR = \int SAR(D')D'^3 g(D')dD' / \int D'^3 g(D')dD'$. Here, g is the number distribution constructed from the TEM mean and standard deviation reported for these cores in [15], 15.3 ± 3.4 nm ($\sigma_{ln} = 0.22$). The integral is evaluated with the trapezoidal rule over $\pm 5\sigma_{ln}$ in ln D (41 nodes; 81 nodes change it by less than 0.1%), and K_{eff} is kept at its fitted value for all sizes. Because K_{eff} was obtained in [15] with a single core size, the monodisperse case remains the reference, and the width of the distribution enters the uncertainty analysis (Section 4.6).

For comparison, LRT gives

$$SAR_{LRT} = \frac{\pi\mu_0\chi_0 f {H_0}^2}{\rho_{Fe_3O_4}}\,\frac{2\pi f\tau_N}{1 + (2\pi f\tau_N)^2},$$
$$\chi_0 = \frac{\mu_0 {M_s}^2 V}{3k_B T}, \qquad \xi = \frac{\mu_0 M_s V H_0}{k_B T} \tag{4}$$

LRT was used only as a diagnostic and is shown in Figure 2 only where $\xi < 1$ [11]. The barrier height tables were calculated at 641 points in the reduced magnetic field ($|h|$

≤ 1.6) and 1440 angles, employing parabolic refinement near the extrema. Equation (2) was integrated over one cycle using an exponential integrator (400 steps per cycle, with linear interpolation of the equilibrium occupations within each step). The loop area integral of Equation (3) matched the direct numerical integration of the dissipated energy to within a relative difference of 10^{-10}. For H_0 = 100 A m^{-1} ($\xi \approx 0.02$), the two-level SAR agreed with LRT to within 0.7%. SAR(H_0, T) was tabulated at 1 K intervals over 35–100 °C, with linear interpolation between the tabulated values; temperatures outside this range terminated the simulation.

4.3. Bioheat Transfer

Heat transport follows the Pennes equation [19] in spherical symmetry,

$$\rho c_{\mathrm{p}} \frac{\partial T}{\partial t} = \frac{1}{r^2}\frac{\partial}{\partial r}\left(k\, r^2 \frac{\partial T}{\partial r}\right) - \omega C_{\mathrm{b}}\,(T - T_a) + q(r,t),$$
$$q(r,t) = \begin{cases} c_{\mathrm{Fe_3O_4}}\,\mathrm{SAR}\big(H_0, T(r,t)\big), & r \le R_{\mathrm{t}},\ t \le t_{\mathrm{on}} \\ 0, & \text{otherwise} \end{cases} \quad (5)$$

Equation (5) uses piecewise-constant properties (tumor for $r \le R_t$ and white matter otherwise; Table 1), with t_{on} = 60 min and the simulation continued to 90 min. Initially, $T(r, 0) = T_a$ = 37 °C, the arterial temperature prescribed in Pennes models of nanoparticle hyperthermia [21]. At r = 0, a symmetry (zero-flux) condition is imposed; at $r = R_t$, temperature and heat flux are continuous, while $T = T_a$ is imposed at $r = R_{max} = R_t + 10L_h$, where $L = (k/\omega C_b)^{1/2}$ is the perfusion length (L_t = 5.0 mm, L_h = 5.6 mm). Since the model describes the rise relative to the arterial baseline, the metabolic heat term does not appear. R_t is the radius of the equivalent sphere, $R_t = (3V_t/4\pi)^{1/3}$. We used a cell-centered finite-volume method (80 cells within the tumor, identical cell spacing outside, and the boundary positioned at a cell face), harmonic-mean face thermal conductivities, implicit Euler time discretization (Δt = 0.5 s), a magnetic source term lagged by one time step, and coupling of the outermost cell to the boundary condition using the conductance across half a cell width. Verification included evaluation of the relative energy-balance residual (energy stored = energy deposited by the magnetic field − energy removed by perfusion − energy transferred by thermal conduction) both within the tumor and over the entire computational domain; this residual did not exceed 2.1×10^{-14}. The thermal-balance residual for the central cell did not exceed 1.0×10^{-14} K s^{-1}. The steady-state solution was obtained by Picard iteration on SAR(T) with a convergence tolerance of 10^{-9} K.

In the sensitivity cases of Sections 2.5 and 2.8, perfusion and conductivity depend on temperature. Tumor perfusion follows the relative form of the function of Lang et al., as given in [38]: $(\omega C_b)_t(T) = (\omega C_b)_{t,0}[0.833 - (T - 37)^{4.8}/5438]/0.833$ for $37 \le T \le 42$ °C and $0.50(\omega C_b)_{t,0}$ above 42 °C, i.e., a functional collapse to half of the baseline, while host perfusion keeps its baseline value. As the opposite bounding case, host and tumor perfusion take the hyperthermic increase estimated for healthy brain and tumor (×2.5 and ×1.5) [5]. Both conductivities scale with that of water [26], $k(T) = k(37\ °C)k_w(T)/k_w(37\ °C)$, assuming that conduction in these tissues is dominated by their water content; k then increases by about 4% between 37 and 55 °C. Like the magnetic source, these coefficients are evaluated at the previous time step, and the energy balance uses the same values, so that it remains closed. Temperature-dependent properties of this kind are also used in coupled electromagnetic–thermal planning models [22].

4.4. Thermal Dose and Coverage Metrics

The thermal dose and the constant-temperature equivalent of the tumor-median dose are

$$\mathrm{CEM43}(r,t) = \frac{1}{60}\int_0^t R^{43-T(r,s)}\,ds, \qquad R = \begin{cases} 0.5, & T \geq 43\,^{\circ}\mathrm{C} \\ 0.25, & T < 43\,^{\circ}\mathrm{C} \end{cases}$$
$$T_{\mathrm{eq}} = 43 - \frac{\ln(\mathrm{CEM43}_{50}/60)}{\ln R_{\mathrm{eq}}}, \qquad R_{\mathrm{eq}} = \begin{cases} 0.5, & \mathrm{CEM43}_{50} \geq 60\ \mathrm{min} \\ 0.25, & \mathrm{CEM43}_{50} < 60\ \mathrm{min} \end{cases} \tag{6}$$

where the integration variable s is expressed in seconds and T in °C; the integral was evaluated with the trapezoidal rule. Since $R_{eq} < 1$, the criterion $\mathrm{CEM43}_{50} \geq 60$ min, used to select R_{eq}, is equivalent to $T_{eq} \geq 43$ °C, so the appropriate branch of the piecewise definition of R is applied consistently. T_{50} and $\mathrm{CEM43}_{50}$ refer to the temperature and thermal dose, respectively, exceeded in 50% of the tumor volume. Coverage is the fraction of this volume with CEM43 ≥ 30 min or ≥ 240 min, which correspond to 30 min exposures at 43 °C and 46 °C, the two SH-SY5Y benchmarks [39–41]. All volume metrics use r^2 weighting.

4.5. Steady Perfusion-Limited Relation

The steady-state solution of Equation (5) for a homogeneous heat source q within a sphere of radius R_t embedded in an infinite perfused host medium is obtained analytically. The rise $T - T_a$ is proportional to $1 + a\sinh(r/L_t)/r$ inside the sphere, with a constant a, and to $\exp(-r/L_h)/r$ outside. Matching the temperature and the radial heat flux at $r = R_t$ yields, with $x = R_t/L_t$ and $y = R_t/L_h$,

$$\frac{T(0) - T_{\mathrm{a}}}{q/(\omega C_{\mathrm{b}})_{\mathrm{t}}} = 1 - \frac{x}{\Lambda}, \qquad \frac{T(R_{\mathrm{t}}) - T_a}{q/(\omega C_{\mathrm{b}})_{\mathrm{t}}} = 1 - \frac{\sinh x}{\Lambda},$$
$$\Lambda = \sinh x + \frac{k_{\mathrm{t}}}{k_{\mathrm{h}}}\frac{x\cosh x - \sinh x}{1+y}, \qquad SAR_{\mathrm{req}} = \frac{(T_{\mathrm{thr}} - T_{\mathrm{a}})\,(\omega C_{\mathrm{b}})_{\mathrm{t}}}{c_{Fe_3O_4}} \tag{7}$$

Equation (7) is the closed form of the matching conditions solved in the script. For $x \gg 1$ the center rise tends to $q/(\omega C_b)_t$, so SAR_{req} is the minimum local SAR needed to reach a center temperature T_{thr}.

4.6. Uncertainty and Sensitivity Analysis

Following credibility guidelines for in silico medicine [54], the uncertain inputs were sampled within their literature bounds: τ_0 log-uniformly in 10^{-11}–10^{-9} s [25]; K_{eff} uniformly in 11.7–11.9 kJ m^{-3} [15]; σ_{ln} uniformly between 0 (monodisperse) and the reported width [15]; and the tumor and host perfusion factors uniformly between the temperature-induced collapse [38] and the hyperthermic increase [5], 0.5–1.5 and 1–2.5, respectively. For each sample, $\mathrm{SAR}(H_0, T)$ was taken from a table of the dimensionless two-level loss as a function of σ, h_0 and $2\pi f\tau_0$ (log-linear interpolation; 95th-percentile error 0.4% relative to direct calculation). The steady Pennes problem was then solved, since the temperature plateau is reached within about 10 min (Figure 3). T_{50} is reported as the median and the 5th–95th percentile range of 4000 samples; with 2000 samples, the median changes by about 0.3 K. First-order and total Sobol indices of T_{50} were estimated with the Jansen estimators [55,56] from $N(k + 2)$ model runs ($N = 8192$, $k = 5$ inputs), with bootstrap confidence intervals.

5. Conclusions

The framework computes the heat source from the non-linear dynamic hysteresis of immobilized cores at the local temperature, separates the magnetic source from the constituents that act only through heat transport, and traces every input to a published measurement. For a literature-derived scenario that combines immobilized 15.3 nm magnetite cores, the iron dose and field protocol from the clinical glioblastoma trial, CNS NB-FOXR2

volumes and brain-tumor tissue properties, the model yields five conclusions for this hypothetical case study. First, at the clinical iron dose, the power deposition depends only on the magnetic phase; the ZnO: Fe_3O_4: chitosan ratio modifies the median rise by at most 1.3%. The ratio is therefore a non-thermal design parameter, constrained mainly by the solubility limit of ZnO. Second, at 100 kHz and above about 4 kA m^{-1}, linear response theory is no longer applicable to these cores and overestimates the energy loss by 63% relative to the two-level hysteresis model at the Atkinson–Brezovich field (H_{AB}). Third, heating of the 115 mL tumor is perfusion-limited, so its central rise follows the ratio of the heat source to the perfusion coefficient. The 10.5 mL lesion, by contrast, is limited by conduction to the surroundings, and its center stays below 43 °C at H_{AB}. Fourth, in the 115 mL case, a median of 43 °C (4.9 kA m^{-1}) and 90% coverage with CEM43 ≥ 30 min (6.2 kA m^{-1}) require amplitudes close to or moderately above this exposure criterion, and above about 8 kA m^{-1} heating extends primarily into the adjacent white matter. Finally, the predictions are controlled by the magnetic characterization: τ_0 can change the loss of monodisperse cores by up to two orders of magnitude, a log-normal distribution built from the reported TEM size spread triples it, and together they dominate the Monte Carlo interval of T_{50} at H_{AB} (37–59 °C). A joint measurement of the magnetic relaxation and size distribution of the immobilized formulation, planned as future experimental work, would turn the case study into a quantitative prediction. These conclusions apply to a composite case assembled from different sources and do not validate any specific synthesized formulation.

Author Contributions: Conceptualization: I.A.T., L.B., M.A.I. and A.M.M. (Adrian Mihail Motoc). Methodology: I.A.T., L.B., M.A.I., M.N.C. and A.M.M. (Ana Maria Mocioiu). Software: L.B. and M.N.C. Formal analysis: I.A.T., L.B., M.N.C. and A.M.M. (Ana Maria Mocioiu). Investigation: I.A.T., M.A.I., A.M.M. (Ana Maria Mocioiu) and A.M.M. (Adrian Mihail Motoc). Validation: L.B., M.A.I., M.N.C., A.M.M. (Ana Maria Mocioiu) and A.M.M. (Adrian Mihail Motoc). Data curation: A.M.M. (Ana Maria Mocioiu) and M.N.C. Visualization: M.N.C. and A.M.M. (Adrian Mihail Motoc). Writing—original draft: I.A.T., L.B. and M.A.I. Writing—review & editing: M.A.I., A.M.M. (Ana Maria Mocioiu) and A.M.M. (Adrian Mihail Motoc). Supervision: I.A.T. and A.M.M. (Adrian Mihail Motoc). Project administration: I.A.T. Funding acquisition: A.M.M. (Ana Maria Mocioiu). All authors have read and agreed to the published version of the manuscript.

Funding: The article processing charge (APC) was funded by the Ministry of Research, Innovation and Digitalization of Romania through the Core Program ENERCLEAN, project number PN 23 25 02 02.

Data Availability Statement: All input parameters and their sources are listed in Table 1, and the model equations and numerical settings are provided in the Methods section. The Excel files containing the numerical data generated using MATLAB for the figures, as well as the MATLAB source code, are not publicly available.

Acknowledgments: The authors gratefully acknowledge the Ministry of Research, Innovation and Digitalization of Romania for its financial support through the Core Program ENERCLEAN, project number PN 23 25 02 02, for covering the article processing charge (APC).

Conflicts of Interest: The authors declare no conflict of interest.

References

1. Maier-Hauff, K.; Ulrich, F.; Nestler, D.; Niehoff, H.; Wust, P.; Thiesen, B.; Orawa, H.; Budach, V.; Jordan, A. Efficacy and safety of intratumoral thermotherapy using magnetic iron-oxide nanoparticles combined with external beam radiotherapy on patients with recurrent glioblastoma multiforme. *J. Neurooncol.* **2011**, *103*, 317–324. https://doi.org/10.1007/s11060-010-0389-0.
2. Skandalakis, G.P.; Rivera, D.R.; Rizea, C.D.; Bouras, A.; Raj, J.G.J.; Bozec, D.; Hadjipanayis, C.G. Hyperthermia treatment advances for brain tumors. *Int. J. Hyperth.* **2020**, *37*, 3–19. https://doi.org/10.1080/02656736.2020.1772512.

3. Rubia-Rodríguez, I.; Santana-Otero, A.; Spassov, S.; Tombácz, E.; Johansson, C.; De La Presa, P.; Teran, F.J.; Morales, M.d.P.; Veintemillas-Verdaguer, S.; Thanh, N.T.K.; et al. Whither magnetic hyperthermia? A tentative roadmap. *Materials* **2021**, *14*, 706. https://doi.org/10.3390/ma14040706.
4. Rentzeperis, F.; Rivera, D.; Zhang, J.Y.; Brown, C.; Young, T.; Rodriguez, B.; Schupper, A.; Price, G.; Gomberg, J.; Williams, T.; et al. Recent developments in magnetic hyperthermia therapy (MHT) and magnetic particle imaging (MPI) in the brain tumor field: A scoping review and meta-analysis. *Micromachines* **2024**, *15*, 559. https://doi.org/10.3390/mi15050559.
5. Schooneveldt, G.; Dobšíček Trefná, H.; Persson, M.; de Reijke, T.M.; Blomgren, K.; Kok, H.P.; Crezee, H. Hyperthermia treatment planning including convective flow in cerebrospinal fluid for brain tumour hyperthermia treatment using a novel dedicated paediatric brain applicator. *Cancers* **2019**, *11*, 1183. https://doi.org/10.3390/cancers11081183.
6. Eivazzadeh-Keihan, R.; Pajoum, Z.; Aliabadi, H.A.M.; Mohammadi, A.; Kashtiaray, A.; Bani, M.S.; Pishva, B.; Maleki, A.; Heravi, M.M.; Mahdavi, M.; et al. Magnetized chitosan hydrogel and silk fibroin, reinforced with PVA: A novel nanobiocomposite for biomedical and hyperthermia applications. *RSC Adv.* **2023**, *13*, 8540–8550. https://doi.org/10.1039/D3RA00612C.
7. Pan, C.-Y.; Lin, F.-Y.; Kao, L.-S.; Huang, C.-C.; Liu, P.-S. Zinc oxide nanoparticles modulate the gene expression of ZnT1 and ZIP8 to manipulate zinc homeostasis and stress-induced cytotoxicity in human neuroblastoma SH-SY5Y cells. *PLoS ONE* **2020**, *15*, e0232729. https://doi.org/10.1371/journal.pone.0232729.
8. Biedler, J.L.; Helson, L.; Spengler, B.A. Morphology and growth, tumorigenicity, and cytogenetics of human neuroblastoma cells in continuous culture. *Cancer Res.* **1973**, *33*, 2643–2652. PMID: 4748425. https://pubmed.ncbi.nlm.nih.gov/4748425/.
9. Mu, Q.; David, C.A.; Galceran, J.; Rey-Castro, C.; Krzemiński, Ł.; Wallace, R.; Bamiduro, F.; Milne, S.J.; Hondow, N.S.; Brydson, R.; et al. Systematic investigation of the physicochemical factors that contribute to the toxicity of ZnO nanoparticles. *Chem. Res. Toxicol.* **2014**, *27*, 558–567. https://doi.org/10.1021/tx4004243.
10. Rosensweig, R.E. Heating magnetic fluid with alternating magnetic field. *J. Magn. Magn. Mater.* **2002**, *252*, 370–374. https://doi.org/10.1016/S0304-8853(02)00706-0.
11. Carrey, J.; Mehdaoui, B.; Respaud, M. Simple models for dynamic hysteresis loop calculations of magnetic single-domain nanoparticles: Application to magnetic hyperthermia optimization. *J. Appl. Phys.* **2011**, *109*, 083921. https://doi.org/10.1063/1.3551582.
12. Stoner, E.C.; Wohlfarth, E.P. A mechanism of magnetic hysteresis in heterogeneous alloys. *Phil. Trans. R. Soc. Lond. A* **1948**, *240*, 599–642. https://doi.org/10.1098/rsta.1948.0007.
13. Brown, W.F., Jr. Thermal fluctuations of a single-domain particle. *Phys. Rev.* **1963**, *130*, 1677–1686. https://doi.org/10.1103/PhysRev.130.1677.
14. Ruta, S.; Chantrell, R.; Hovorka, O. Unified model of hyperthermia via hysteresis heating in systems of interacting magnetic nanoparticles. *Sci. Rep.* **2015**, *5*, 9090. https://doi.org/10.1038/srep09090.
15. García-Acevedo, P.; González-Gómez, M.A.; Arnosa-Prieto, Á.; de Castro-Alves, L.; Piñeiro, Y.; Rivas, J. Role of dipolar interactions on the determination of the effective magnetic anisotropy in iron oxide nanoparticles. *Adv. Sci.* **2023**, *10*, 2203397. https://doi.org/10.1002/advs.202203397.
16. Ait Kerroum, M.A.; Iacovita, C.; Baaziz, W.; Ihiawakrim, D.; Rogez, G.; Benaissa, M.; Lucaciu, C.M.; Ersen, O. Quantitative analysis of the specific absorption rate dependence on the magnetic field strength in $Zn_xFe_{3-x}O_4$ nanoparticles. *Int. J. Mol. Sci.* **2020**, *21*, 7775. https://doi.org/10.3390/ijms21207775.
17. Cabrera, D.; Coene, A.; Leliaert, J.; Artés-Ibáñez, E.J.; Dupré, L.; Telling, N.D.; Teran, F.J. Dynamical magnetic response of iron oxide nanoparticles inside live cells. *ACS Nano* **2018**, *12*, 2741–2752. https://doi.org/10.1021/acsnano.7b08995.
18. Garaio, E.; Sandre, O.; Collantes, J.-M.; Garcia, J.A.; Mornet, S.; Plazaola, F. Specific absorption rate dependence on temperature in magnetic field hyperthermia measured by dynamic hysteresis losses (ac magnetometry). *Nanotechnology* **2015**, *26*, 015704. https://doi.org/10.1088/0957-4484/26/1/015704.
19. Pennes, H.H. Analysis of tissue and arterial blood temperatures in the resting human forearm. *J. Appl. Physiol.* **1948**, *1*, 93–122. https://doi.org/10.1152/jappl.1948.1.2.93.
20. Rytov, R.A.; Bautin, V.A.; Usov, N.A. Towards optimal thermal distribution in magnetic hyperthermia. *Sci. Rep.* **2022**, *12*, 3023. https://doi.org/10.1038/s41598-022-07062-1.
21. LeBrun, A.; Ma, R.; Zhu, L. MicroCT image based simulation to design heating protocols in magnetic nanoparticle hyperthermia for cancer treatment. *J. Therm. Biol.* **2016**, *62*, 129–137. https://doi.org/10.1016/j.jtherbio.2016.06.025.
22. Lodi, M.B.; Curreli, N.; Zappia, S.; Pilia, L.; Casula, M.F.; Fiorito, S.; Catapano, I.; Desogus, F.; Pellegrino, T.; Kriegel, I.; et al. Influence of magnetic scaffold loading patterns on their hyperthermic potential against bone tumors. *IEEE Trans. Biomed. Eng.* **2022**, *69*, 2029–2040. https://doi.org/10.1109/TBME.2021.3134208.

23. Tietze, A.; Mankad, K.; Lequin, M.H.; Ivarsson, L.; Mirsky, D.; Jaju, A.; Kool, M.; Hoff, K.V.; Bison, B.; Löbel, U. Imaging characteristics of CNS neuroblastoma-FOXR2: A retrospective and multi-institutional description of 25 cases. *AJNR Am. J. Neuroradiol.* **2022**, *43*, 1476–1480. https://doi.org/10.3174/ajnr.A7644.
24. Suriyanto; Ng, E.Y.K.; Kumar, S.D. Physical mechanism and modeling of heat generation and transfer in magnetic fluid hyperthermia through Néelian and Brownian relaxation: A review. *Biomed. Eng. Online* **2017**, *16*, 36. https://doi.org/10.1186/s12938-017-0327-x.
25. Goya, G.F.; Fonseca, F.C.; Jardim, R.F.; Muccillo, R.; Carreño, N.L.V.; Longo, E.; Leite, E.R. Magnetic dynamics of single-domain Ni nanoparticles. *J. Appl. Phys.* **2003**, *93*, 6531–6533. https://doi.org/10.1063/1.1540032.
26. Ramires, M.L.V.; Nieto de Castro, C.A.; Nagasaka, Y.; Nagashima, A.; Assael, M.J.; Wakeham, W.A. Standard reference data for the thermal conductivity of water. *J. Phys. Chem. Ref. Data* **1995**, *24*, 1377–1381. https://doi.org/10.1063/1.555963.
27. Ahuja, A.S.; Prasad, K.N.; Hendee, W.R.; Carson, P.L. Thermal conductivity and diffusivity of neuroblastoma tumor cells. *Med. Phys.* **1978**, *5*, 418–421. https://doi.org/10.1118/1.594434.
28. Shimazaki, K.; Kurokawa, R.; Franson, A.; Kurokawa, M.; Baba, A.; Bou-Maroun, L.; Kim, J.; Moritani, T. Neuroimaging features of FOXR2-activated CNS neuroblastoma: A case series and systematic review. *J. Neuroimaging* **2023**, *33*, 359–367. https://doi.org/10.1111/jon.13095.
29. Singh, S.; Bianchi, L.; Korganbayev, S.; Namakshenas, P.; Melnik, R.; Saccomandi, P. Non-Fourier bioheat transfer analysis in brain tissue during interstitial laser ablation: Analysis of multiple influential factors. *Ann. Biomed. Eng.* **2024**, *52*, 967–981. https://doi.org/10.1007/s10439-023-03433-5.
30. Atkinson, W.J.; Brezovich, I.A.; Chakraborty, D.P. Usable frequencies in hyperthermia with thermal seeds. *IEEE Trans. Biomed. Eng.* **1984**, *31*, 70–75. https://doi.org/10.1109/TBME.1984.325372.
31. Hergt, R.; Dutz, S. Magnetic particle hyperthermia—Biophysical limitations of a visionary tumour therapy. *J. Magn. Magn. Mater.* **2007**, *311*, 187–192. https://doi.org/10.1016/j.jmmm.2006.10.1156.
32. Herrero de la Parte, B.; Rodrigo, I.; Gutiérrez-Basoa, J.; Iturrizaga Correcher, S.; Mar Medina, C.; Echevarría-Uraga, J.J.; Garcia, J.A.; Plazaola, F.; García-Alonso, I. Proposal of new safety limits for in vivo experiments of magnetic hyperthermia antitumor therapy. *Cancers* **2022**, *14*, 3084. https://doi.org/10.3390/cancers14133084.
33. Gneveckow, U.; Jordan, A.; Scholz, R.; Brüß, V.; Waldöfner, N.; Ricke, J.; Feussner, A.; Hildebrandt, B.; Rau, B.; Wust, P. Description and characterization of the novel hyperthermia- and thermoablation-system MFH 300F for clinical magnetic fluid hyperthermia. *Med. Phys.* **2004**, *31*, 1444–1451. https://doi.org/10.1118/1.1748629.
34. Behrends, A.; Wei, H.; Neumann, A.; Friedrich, T.; Bakenecker, A.C.; Franke, J.; Sajjamark, K.; Buchholz, O.; Bär, S.; Hofmann, U.G.; et al. Integrable magnetic fluid hyperthermia systems for 3D magnetic particle imaging. *Nanotheranostics* **2024**, *8*, 163–178. https://doi.org/10.7150/ntno.90360.
35. Sapareto, S.A.; Dewey, W.C. Thermal dose determination in cancer therapy. *Int. J. Radiat. Oncol. Biol. Phys.* **1984**, *10*, 787–800. https://doi.org/10.1016/0360-3016(84)90379-1.
36. van Rhoon, G.C.; Samaras, T.; Yarmolenko, P.S.; Dewhirst, M.W.; Neufeld, E.; Kuster, N. CEM43°C thermal dose thresholds: A potential guide for magnetic resonance radiofrequency exposure levels? *Eur. Radiol.* **2013**, *23*, 2215–2227. https://doi.org/10.1007/s00330-013-2825-y.
37. Tiesinga, E.; Mohr, P.J.; Newell, D.B.; Taylor, B.N. CODATA recommended values of the fundamental physical constants: 2018. *Rev. Mod. Phys.* **2021**, *93*, 025010. https://doi.org/10.1103/RevModPhys.93.025010.
38. Maniotis, N.; Mitropoulos, S.; Vordos, N.; Tsiantos, V. The role of blood perfusion in the thermal interaction between magnetic nanoparticles and cancerous tumors: A computational study. *Magnetism* **2025**, *5*, 6. https://doi.org/10.3390/magnetism5010006.
39. Cheng, L.; Smith, D.J.; Anderson, R.L.; Nagley, P. Modulation of cellular Hsp72 levels in undifferentiated and neuron-like SH-SY5Y cells determines resistance to staurosporine-induced apoptosis. *PLoS ONE* **2011**, *6*, e24473. https://doi.org/10.1371/journal.pone.0024473.
40. Cheng, L.; Smith, D.J.; Anderson, R.L.; Nagley, P. Human neuroblastoma SH-SY5Y cells show increased resistance to hyperthermic stress after differentiation, associated with elevated levels of Hsp72. *Int. J. Hyperth.* **2011**, *27*, 415–426. https://doi.org/10.3109/02656736.2010.531075.
41. Sanz, B.; Calatayud, M.P.; Torres, T.E.; Fanarraga, M.L.; Ibarra, M.R.; Goya, G.F. Magnetic hyperthermia enhances cell toxicity with respect to exogenous heating. *Biomaterials* **2017**, *114*, 62–70. https://doi.org/10.1016/j.biomaterials.2016.11.008.
42. Baumann, S.B.; Wozny, D.R.; Kelly, S.K.; Meno, F.M. The electrical conductivity of human cerebrospinal fluid at body temperature. *IEEE Trans. Biomed. Eng.* **1997**, *44*, 220–223. https://doi.org/10.1109/10.554770.

43. Hasgall, P.A.; Di Gennaro, F.; Baumgartner, C.; Neufeld, E.; Lloyd, B.; Gosselin, M.C.; Payne, D.; Klingenböck, A.; Kuster, N. *IT'IS Database for Thermal and Electromagnetic Parameters of Biological Tissues*, Version 4.1; IT'IS Foundation: Zurich, Switzerland, 2022. https://doi.org/10.13099/VIP21000-04-1.
44. Coffey, W.T.; Kalmykov, Y.P. Thermal fluctuations of magnetic nanoparticles: Fifty years after Brown. *J. Appl. Phys.* **2012**, *112*, 121301. https://doi.org/10.1063/1.4754272.
45. Branquinho, L.C.; Carrião, M.S.; Costa, A.S.; Zufelato, N.; Sousa, M.H.; Miotto, R.; Ivkov, R.; Bakuzis, A.F. Effect of magnetic dipolar interactions on nanoparticle heating efficiency: Implications for cancer hyperthermia. *Sci. Rep.* **2013**, *3*, 2887. https://doi.org/10.1038/srep02887.
46. Huber, M.L.; Perkins, R.A.; Laesecke, A.; Friend, D.G.; Sengers, J.V.; Assael, M.J.; Metaxa, I.N.; Vogel, E.; Mareš, R.; Miyagawa, K. New international formulation for the viscosity of H_2O. *J. Phys. Chem. Ref. Data* **2009**, *38*, 101–125. https://doi.org/10.1063/1.3088050.
47. Rabin, Y. Is intracellular hyperthermia superior to extracellular hyperthermia in the thermal sense? *Int. J. Hyperth.* **2002**, *18*, 194–202. https://doi.org/10.1080/02656730110116713.
48. Lodi, M.B.; Possidente, R.; Melis, A.; Di Meglio, A.; Fanti, A.; Baccoli, R. Thermal behavior of magnetic scaffolds for RF-induced hyperthermia. *Appl. Sci.* **2025**, *15*, 9782. https://doi.org/10.3390/app15179782.
49. van Rhoon, G.C. Is CEM43 still a relevant thermal dose parameter for hyperthermia treatment monitoring? *Int. J. Hyperth.* **2016**, *32*, 50–62. https://doi.org/10.3109/02656736.2015.1114153.
50. Prohaska, T.; Irrgeher, J.; Benefield, J.; Böhlke, J.K.; Chesson, L.A.; Coplen, T.B.; Ding, T.; Dunn, P.J.H.; Gröning, M.; Holden, N.E.; et al. Standard atomic weights of the elements 2021 (IUPAC Technical Report). *Pure Appl. Chem.* **2022**, *94*, 573–600. https://doi.org/10.1515/pac-2019-0603.
51. Pearton, S.J.; Norton, D.P.; Ip, K.; Heo, Y.W.; Steiner, T. Recent advances in processing of ZnO. *J. Vac. Sci. Technol. B* **2004**, *22*, 932–948. https://doi.org/10.1116/1.1714985.
52. Eapen, J.; Rusconi, R.; Piazza, R.; Yip, S. The classical nature of thermal conduction in nanofluids. *J. Heat Transf.* **2010**, *132*, 102402. https://doi.org/10.1115/1.4001304.
53. Hashin, Z.; Shtrikman, S. A variational approach to the theory of the effective magnetic permeability of multiphase materials. *J. Appl. Phys.* **1962**, *33*, 3125–3131. https://doi.org/10.1063/1.1728579.
54. Viceconti, M.; Pappalardo, F.; Rodriguez, B.; Horner, M.; Bischoff, J.; Musuamba Tshinanu, F. In silico trials: Verification, validation and uncertainty quantification of predictive models used in the regulatory evaluation of biomedical products. *Methods* **2021**, *185*, 120–127. https://doi.org/10.1016/j.ymeth.2020.01.011.
55. Saltelli, A.; Annoni, P.; Azzini, I.; Campolongo, F.; Ratto, M.; Tarantola, S. Variance based sensitivity analysis of model output. Design and estimator for the total sensitivity index. *Comput. Phys. Commun.* **2010**, *181*, 259–270. https://doi.org/10.1016/j.cpc.2009.09.018.
56. Jansen, M.J.W. Analysis of variance designs for model output. *Comput. Phys. Commun.* **1999**, *117*, 35–43. https://doi.org/10.1016/S0010-4655(98)00154-4.

Disclaimer/Publisher's Note: The statements, opinions and data contained in all publications are solely those of the individual author(s) and contributor(s) and not of MDPI and/or the editor(s). MDPI and/or the editor(s) disclaim responsibility for any injury to people or property resulting from any ideas, methods, instructions or products referred to in the content.